NANO LETTERS

pubs.acs.org/NanoLett

Letter

Percolation of Ion-Irradiation-Induced Disorder in Complex Oxide Interfaces

Bethany E. Matthews, Michel Sassi, Christopher Barr, Colin Ophus, Tiffany C. Kaspar, Weilin Jiang, Khalid Hattar, and Steven R. Spurgeon*

Cite This: *Nano Lett.* 2021, 21, 5353−5359

Read Online

ACCESS | Metrics & More | Article Recommendations | Supporting Information

ABSTRACT: Mastery of order−disorder processes in highly nonequilibrium nanostructured oxides has significant implications for the development of emerging energy technologies. However, we are presently limited in our ability to quantify and harness these processes at high spatial, chemical, and temporal resolution, particularly in extreme environments. Here, we describe the percolation of disorder at the model oxide interface $LaMnO_3$/$SrTiO_3$, which we visualize during *in situ* ion irradiation in the transmission electron microscope. We observe the formation of a network of disorder during the initial stages of ion irradiation and track the global progression of the system to full disorder. We couple these measurements with detailed structural and chemical probes, examining possible underlying defect mechanisms responsible for this unique percolative behavior.

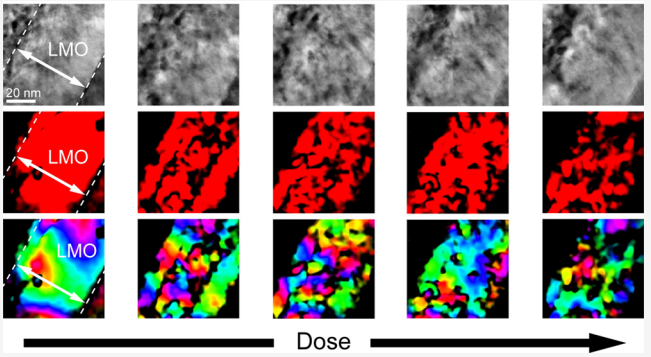

KEYWORDS: *order−disorder, oxide interfaces, ion irradiation, in situ transmission electron microscopy, density functional theory*

INTRODUCTION

Interface engineering of oxide thin films is one of the great achievements of materials science, underpinning exotic physics[1] and giving rise to advanced computing and energy technologies.[2] Because of strong interplay among lattice, charge, and spin degrees of freedom, even slight fluctuations in local order at oxide interfaces can greatly impact behaviors such as electronic[3] and ionic conductivity.[4] Order can be disrupted via numerous defect mechanisms, such as local structural perturbations[5,6] or the formation of cation and anion vacancies.[7,8] The class of manganite perovskite oxides, such as $LaMnO_3$, has attracted particular attention in this context since electronic, magnetic, and optical properties are closely coupled to lattice structure and defects.[9−11] The desire to understand these mechanisms has motivated efforts to map defect formation pathways during oxide synthesis[12,13] and exposure to extreme environments.[14−16] Understanding oxides in extremes of temperature and irradiation is particularly important, since devices such as solid oxide fuel cells (SOFCs),[6,17] durable nuclear waste forms,[18,19] and space-based electronics[20] must deliver reliable long-term performance under challenging conditions. At a more fundamental level, the nature of order−disorder processes represents a grand scientific question with implications for the design of high entropy alloys[21] and ceramics,[22] strongly correlated quantum systems[23] and more.

To dictate order−disorder behavior, we must be able to visualize and direct defect formation processes at high spatial, chemical, and temporal resolution. The community has a long, successful history of using tailored ion irradiation to manipulate and induce defect populations in bulk metals[24,25] and oxides.[19,26−29] While recent studies[15,16,30,31] have showcased the promising properties of nanostructured systems, such as enhanced defect annihilation at grain boundary sinks[32] leading to radiation hardness, past work has focused almost exclusively on metals and bulk oxides.[15] A handful of studies of model oxide heterointerfaces have combined controlled ion irradiation and local characterization tools to identify unique behaviors, such as antisite defect buildup,[33] oxygen vacancy formation,[34] and orientation-/chemistry-dependent amorphization behavior.[35−37] These studies show that there is an interplay between defect formation energy, which depends on the interface configuration (e.g., strain, charge state, chemistry),[34,36−39] and defect kinetics, particularly defect mobility in different interface components.[40] However, most prior work has focused on static snapshots of these materials and has

Received: April 26, 2021
Revised: June 4, 2021
Published: June 10, 2021

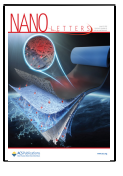

https://doi.org/10.1021/acs.nanolett.1c01651
Nano Lett. 2021, 21, 5353−5359

lacked sufficient spatiotemporal resolution to probe the kinetics of local defect formation, particularly during the initial loss of crystallinity in oxide thin films.

Moving beyond traditional static characterization approaches toward *in situ* methods will allow us to capture the initial onset and evolution of local defects. *In situ* (scanning) transmission electron microscopy ((S)TEM) has been widely employed by the radiation effects community to examine defects in materials,[41−45] providing an invaluable window into irradiation-induced disorder, particularly in the low dose regime. These methods have long been used to examine bulk ceramics,[44,46−49] revealing radiation-induced defect formation pathways and kinetics. Local (S)TEM probes are particularly well-suited to examining nanostructured oxide interfaces,[50] whose nonequilibrium behavior can deviate greatly from bulk materials, but surprisingly little work has been done on complex oxide thin film systems in the context of radiation damage. More broadly, the microscopy community has also recognized the need for new data-driven approaches to characterization of transient processes, needed to detect and quantify salient features during high-speed imaging.[51−53]

Here, we visualize the evolution of local disorder at a $LaMnO_3$ (LMO)/$SrTiO_3$ (STO) (001) perovskite oxide interface using ion irradiation coupled with *in situ* high-resolution transmission electron microscopy (HRTEM) imaging at the I^{3}TEM irradiation facility at Sandia National Laboratories. These interfaces can be synthesized with a high degree of precision, providing an excellent testbed to evaluate ion-irradiation-induced disorder. We observe the initial onset of disorder and track its progression over continued irradiation. Using a Fourier filtering time series approach, we show that initial radiation damage is accommodated by the percolation of amorphous regions throughout the crystalline LMO matrix. In addition, we find evidence for a preserved crystalline interface region even at the highest fluence studied, whose origin we examine in the context of electronic structure calculations and past work. Taken together, these results demonstrate the power of high-resolution *in situ* approaches to derive complex disordering pathways at oxide interfaces. More broadly, the data processing approaches we demonstrate may be applied to other dynamic studies of complex materials phase transitions.

RESULTS AND DISCUSSION

We first consider the overall degradation of the system from a crystalline, as-grown condition to a disordered state. Figure 1A shows the configuration of the electron and ion beams during irradiation, with the sample inclined 30° in the X tilt direction to minimize shadowing of the ion beam. In this geometry, both the LMO and STO layers are illuminated by the ion beam simultaneously. Figure 1B shows a cross-sectional STEM-HAADF image of the starting epitaxial 40 nm LMO film along the STO [100] crystallographic zone-axis prior to irradiation. In this mode, the directly interpretable atomic number ($Z^{\sim 1.7}$) contrast reveals a clear difference between the film and substrate, with minimal intermixing, excellent epitaxy, and no extended defects. Figure 1C shows an HRTEM image of the same film in the I^{3}TEM system, with the interface rotated approximately 60° about the [100] zone (the normal direction to the image plane). Phase contrast in HRTEM is less directly interpretable than STEM-HAADF, but the inset fast Fourier transform (FFT) and clear lattice fringes confirm the crystalline starting condition. From this point, a series of four irradiations were performed in 1 h increments with 2.8

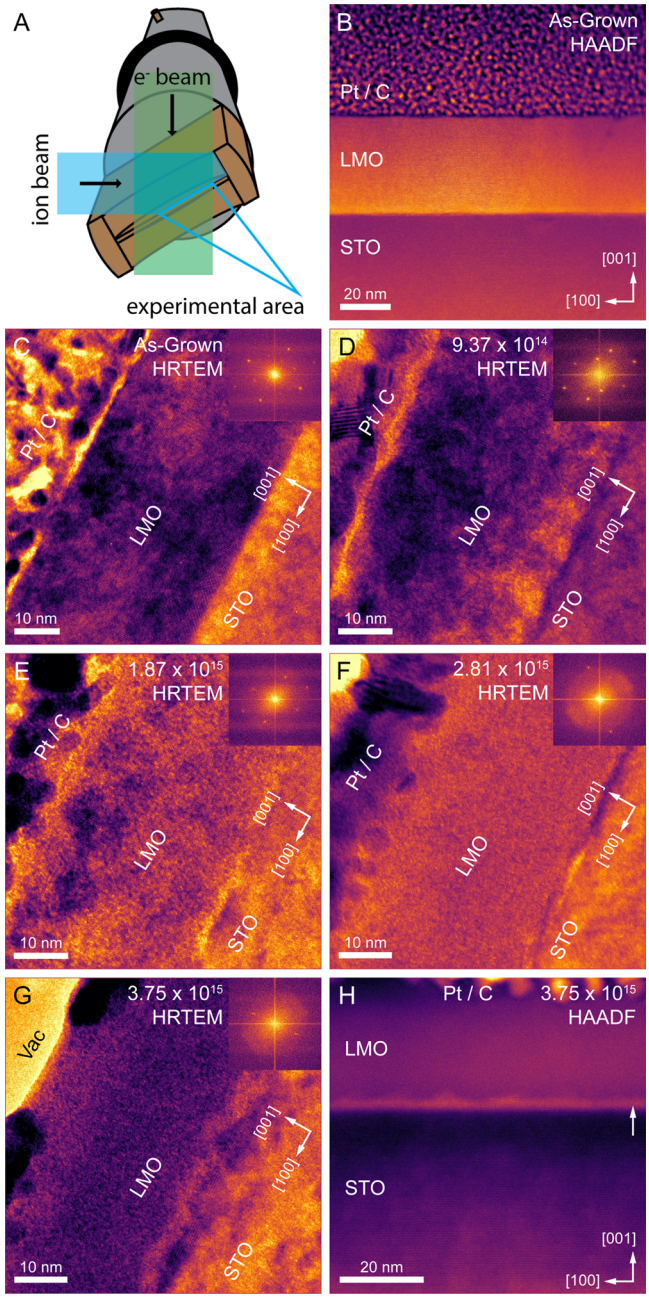

Figure 1. Evolution of local disorder with fluence. (A) Schematic of the irradiation geometry. (B,C) Colorized cross-sectional STEM-HAADF and HRTEM images of the as-grown film. (D−G) HRTEM images for fluences of 9.37×10^{14}, 1.87×10^{15}, 2.81×10^{15}, 3.75×10^{15} Au^{4+} cm^{-2}, respectively. (H) STEM-HAADF image of the 3.75×10^{15} Au^{4+} cm^{-2} fluence sample. (Higher-resolution images are provided in Supporting Information Note 5.)

MeV Au^{4+} ions, as shown in Figure 1D−G, with the sample inclined during irradiation and then tilted back to the zone for imaging. Each irradiation step corresponds to a fluence of 9.37×10^{14} Au^{4+} cm^{-2}. These figures show a gradual amorphization sequence, starting from the LMO film and extending to the STO substrate. A careful inspection of the images and associated FFTs reveals the emergence of local amorphous patches in the LMO at a fluence of 9.37×10^{14} Au^{4+} cm^{-2} (Figure 1D), with less apparent damage in the STO film. By a fluence of 1.87×10^{15} Au^{4+} cm^{-2} (Figure 1E), the patches have grown more extensive in the LMO and the STO side also

https://doi.org/10.1021/acs.nanolett.1c01651
Nano Lett. 2021, 21, 5353−5359

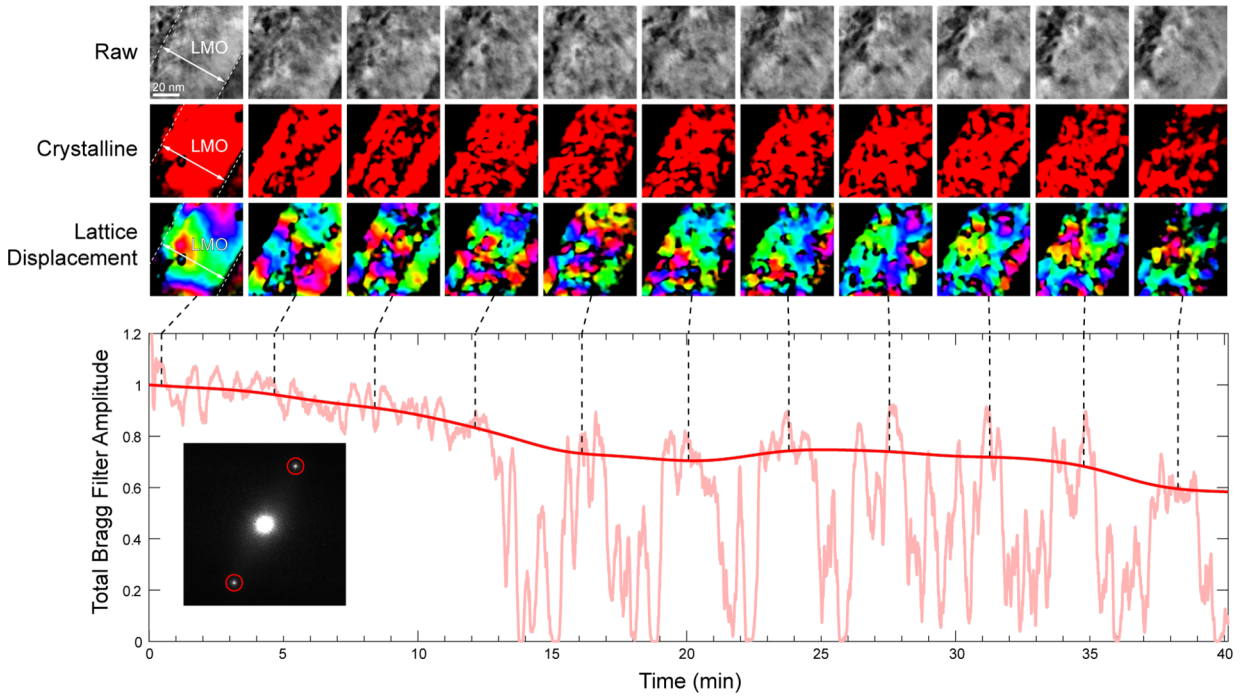

Figure 2. Percolation of initial local lattice disorder. Top to bottom: Raw frames, crystallinity maps, displacement maps, and total Bragg filter amplitude as a function of frame time. The dark red line corresponds to an iteratively fitted time-average of the amplitude data and the inset shows the masked FFT reflections used for the analysis. Total combined fluence over 40 min is 6.25×10^{14} Au^{4+} cm^{-2}.

exhibits obvious disorder; this is accompanied by a decrease in the intensity of the FFT reflections. At a fluence of 2.81×10^{15} Au^{4+} cm^{-2} (Figure 1F), the LMO film is almost entirely amorphous, except for a thin, several nanometers thick band at the interface. Finally, at a fluence of 3.75×10^{15} Au^{4+} cm^{-2} (Figure 1G), the LMO film appears similarly disordered to its state at a fluence of 2.81×10^{15} Au^{4+} cm^{-2}, but it is clearly thinner in the beam direction (as indicated by the larger vacuum region at the top left corner of the image), likely due to sputtering of the film under the ion bombardment. In addition, the STO layer is extensively damaged and the only remaining lattice fringes are from a 2−3 nm band at the film−substrate interface. There is almost no periodic signal left in the FFT, reflecting the loss of overall crystalline order. STEM-HAADF images of the 3.75×10^{15} Au^{4+} cm^{-2} condition (Figure 1H) show that some lattice fringes are still present in the bulk of the STO, but the bulk of the LMO is completely amorphous. Nonetheless, there is a pronounced and persistent crystalline band on the film side of the interface (marked by the arrow).

While many heavy ion species have been effectively used for radiation effects studies, including Kr and Au, we have chosen the latter species and an ion energy peak just through the film to maximize damage per ion strike and subsequent ability to rapidly induce amorphization. This selection creates a minor potential for increased sputtering and some implantation in the bulk, as discussed in Supporting Information Note 3. However, a similar irradiation response has been observed in the $La_2Ti_2O_7$/STO system,[34] where a 5−10 nm crystalline band persisted on the STO side of the interface. While the origins and mechanisms leading to the resistant interface behavior are not fully clear, we do note the presence of some cation intermixing in the irradiated sample (shown in Supporting Information Note 4), which may also affect its stability. Overall, this behavior points to the broader trend for perovskite oxide interface systems to remain crystalline under irradiation environments.

We focus next on the initial stages of the irradiation process, probing the initial percolation of disorder and its buildup to the more global amorphization shown in Figure 1H. For this experiment, we captured a high-speed time series with the sample inclined at 30° in the X tilt direction to maximize exposure to the ion beam. At this high tilt angle, it is no longer possible to directly resolve atomic columns in the [100] zone-axis, and we instead image (100)-type lattice planes. However, the remarkable stability of the sample during the extended period of irradiation (40 min, total fluence 6.25×10^{14} Au^{4+} cm^{-2}) provided a unique window into the initial stages of disorder. We employ a temporal Fourier filtering approach, analogous to time-resolved geometric phase analysis (GPA),[54] processing the raw movie frames into maps of local crystallinity and lattice displacement. In addition, we quantify the total Bragg filter amplitude, which effectively measures the spatial abundance of the selected (100)-type lattice domains in any given frame. It is important to note that, while the overall sample was quite stable, these measurements are very challenging and some periodic bending/rotation of the sample due to local heating did occur; since this results in large, random drops in the Bragg filter amplitude, a trend line was fit to the Bragg filter amplitude only where crystalline signal is present (see Supporting Information Methods for details). These measurements are shown in Figure 2 and Supporting Information Movie S1.

We observe a large, initially contiguous block of crystalline region (red), as expected. By 5 min, some disorder emerges in the film, beginning at its center and extending laterally, but the Bragg amplitude is still around 95% of the starting condition. Disorder is accompanied by significant local lattice displacement around the defective regions. At this stage, dislocations emerge that run from the lower left to upper right corner of the

https://doi.org/10.1021/acs.nanolett.1c01651
Nano Lett. 2021, 21, 5353−5359

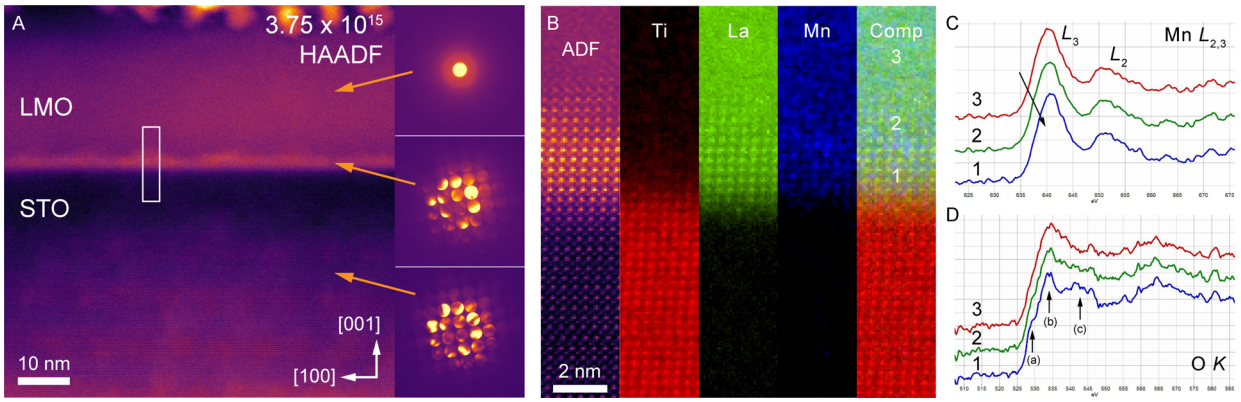

Figure 3. Detail of the interface after irradiation. (A) Colorized cross-sectional STEM-HAADF image with local PACBED patterns from the film, interface, and substrate, taken from the 3.75 × 10^{15} Au^{4+} cm^{-2} fluence sample. (B) Colorized STEM-ADF and corresponding STEM-EELS for Ti $L_{2,3}$, La $M_{4,5}$, Mn $L_{2,3}$, and composite maps taken from near the boxed region in (A). (C–D) Corresponding Mn $L_{2,3}$ and O *K* spectra, respectively, from Regions 1–3.

frames. Between 9 and 19 min, the percolation extends from the film center to its surface and the substrate interface. At this point, there is a substantial drop in the Bragg amplitude to nearly 80%, accompanied by a still more complex pattern of lattice rotation and crystalline domains, some <10 nm in size. The dislocations appear to reconnect, forming repaired epitaxial domains, but there is a clear increase in the fraction of disorder. Between 19 and 33 min the overall distribution remains steady near 80%, but between 33 and 37 min the percolation continues and the crystalline domains become increasingly sparse and disconnected. In the final condition around 40 min, only about 60% of the film is still similar to the starting crystalline condition and there is a large disconnected network of ordered regions. These results point to the highly nonuniform evolution of the interface during the initial stages of irradiation.

To further explore this nonuniform interface response in later stages of irradiation, we have performed local position-averaged convergent beam electron diffraction (PACBED) and electron energy loss spectroscopy (STEM-EELS) measurements. The former is a mode of scanning nanodiffraction[55] that can quantify crystallinity at the nanoscale and has been used before to examine local disorder in oxides,[34,56,57] while the latter has been used to examine chemical states in both pristine and irradiated oxides.[14] As shown in Figure 3A, at a fluence of 3.75 × 10^{15} Au^{4+} cm^{-2} the bulk of the LMO film has amorphized, resulting in a diffuse, ringlike PACBED pattern. In contrast, PACBED from the uniform ∼3 nm interface band exhibits strong diffraction disks; there is also evidence for more weakly diffracting patches that extend further into the film. Similarly, the STO side of the interface also exhibits strong diffraction disks, despite some distributed damage, consistent with past observations.[47,58] Correlative STEM-EELS chemical analysis of the interface, shown in Figure 3B, reveals the gradual breakup of the crystalline film upon transitioning from the interface into the bulk, resulting in three distinct regions (labeled 1–3). Region (1) consists of a ∼3 nm region of LMO that is strongly diffracting and highly chemically ordered on both the La and Mn sublattices. We do note the presence of some oxygen sublattice disorder, as indicated in EELS spectra from this region, which contain a characteristic prepeak (a), main peak (b), and secondary peak (c) in the O *K* edge fine structure (Figure 3C), as well as a clear Mn $L_{2,3}$ white-line doublet (Figure 3D), consistent with previous observations.[11,59] Moving away from the interface and into the LMO, we move into a more weakly diffracting ∼2 nm Region (2) consisting of more poorly defined perovskite atomic order. This region exhibits a reduction in the O *K* prepeak feature and loss of definition between the main and secondary peaks. In addition, there is a clear 0.5 eV shift of the Mn edge to lower energy loss, pointing toward underlying reduction. This region is followed by third and final amorphous region (3) with no extended ordering of La and Mn; now the O *K* edge prepeak has disappeared and the main edge features have blurred into one from the increased randomization of the sublattice. There is a further 0.5 eV Mn chemical shift, reflecting further Mn reduction (see Supporting Information Note 7 for more detail). The origin of this reduction is likely the loss of oxygen (oxygen vacancy formation) and electronic reconfiguration during the ion irradiation process.[34,36]

In order to understand the energetics of oxygen vacancies at the LMO/STO interface, density functional theory (DFT) calculations have been performed, in which an oxygen vacancy has been introduced at different locations of the LMO/STO interface. These simulations used three different model interface terminations (i.e., two LMO/STO (001) and one LMO/STO (110)), as shown in Supporting Information Note 2. The two (100) interface models were built from the STO (100) substrate orientation, terminated either by SrO or TiO_2, yielding LMO/STO interface configurations with cation rows ordering as (Ti–Sr–Mn–La) and (Sr–Ti–La–Mn), respectively. As shown by the relative energy plots in Supporting Information Note 2, forming an oxygen vacancy on the LMO side of the interface is found to be more favorable than on the STO side. This behavior is likely due to the ability of Mn^{4+} ions to reduce to Mn^{3+} more readily than for Ti^{4+} to reduce to Ti^{3+}. Supporting Information Note 2 also shows that creating an oxygen vacancy at the interface of the Ti-terminated LMO (100)/STO (100) configuration is less favorable than creating it at the Sr-terminated configuration. While the Ti-terminated interface provides a less favorable environment for oxygen vacancy creation compared to the Sr-terminated interface, the formation energy is still similar to that in STO. These results suggest that in the LMO/STO system the mechanisms for interface stabilization are not dominated by the oxygen vacancy creation. Nevertheless, these results overall show a net energy gain of 2 eV for vacancy formation on the LMO side of the interface relative to the STO side. This finding is in

https://doi.org/10.1021/acs.nanolett.1c01651
Nano Lett. 2021, 21, 5353–5359

excellent agreement with the overall trend in the amorphization sequence that we observe experimentally. However, unlike in the case of LTO/STO,[34] no interfacial oxygen vacancy differences were observed to explain the retention of crystallinity at the interface, so the specific characteristics of the damage mechanism are likely different.

CONCLUSIONS

Using an *in situ* imaging approach, we reveal the percolation of disorder in oxide thin film interfaces. Our results indicate the formation of a complex network of amorphization during the initial stages of irradiation, which progresses to global disorder over longer time scales. However, we also observe the preservation of a distinct crystalline interface region on the film side of the LMO/STO interface. Our calculations demonstrate a propensity for defect accumulation in the bulk of the LMO, which likely influences the course of the disordering processes. These results support the general trend toward retention of interfacial crystallinity, which appears to be unique to epitaxial oxides. Collectively, these results demonstrate the untapped potential of high-resolution spatiotemporal probes to survey the complex landscape of disorder and underscore the important role of interface engineering in mediating disordering processes.

ASSOCIATED CONTENT

Supporting Information

The Supporting Information is available free of charge at X. , and a are available. The Supporting Information is available free of charge at https://pubs.acs.org/doi/10.1021/acs.nanolett.1c01651.

Details of methods used, DFT calculations, SRIM calculations, sequence of the irradiation, EELS (PDF)

Movie of the irradiation (MP4)

AUTHOR INFORMATION

Corresponding Author

Steven R. Spurgeon − *Energy and Environment Directorate, Pacific Northwest National Laboratory, Richland, Washington 99352, United States;* orcid.org/0000-0003-1218-839X; Email: steven.spurgeon@pnnl.gov

Authors

Bethany E. Matthews − *Energy and Environment Directorate, Pacific Northwest National Laboratory, Richland, Washington 99352, United States;* orcid.org/0000-0001-7193-2583

Michel Sassi − *Physical and Computational Sciences Directorate, Pacific Northwest National Laboratory, Richland, Washington 99352, United States;* orcid.org/0000-0003-2582-3735

Christopher Barr − *Center for Integrated Nanotechnologies, Sandia National Laboratories, Albuquerque, New Mexico 87195, United States*

Colin Ophus − *NCEM, Molecular Foundry, Lawrence Berkeley National Laboratory, Berkeley, California 94720, United States of America*

Tiffany C. Kaspar − *Physical and Computational Sciences Directorate, Pacific Northwest National Laboratory, Richland, Washington 99352, United States;* orcid.org/0000-0003-2816-7569

Weilin Jiang − *Energy and Environment Directorate, Pacific Northwest National Laboratory, Richland, Washington 99352, United States;* orcid.org/0000-0001-8302-8313

Khalid Hattar − *Center for Integrated Nanotechnologies, Sandia National Laboratories, Albuquerque, New Mexico 87195, United States*

Complete contact information is available at: https://pubs.acs.org/10.1021/acs.nanolett.1c01651

Notes

The authors declare no competing financial interest.

ACKNOWLEDGMENTS

This research was supported by the Nuclear Processing Science Initiative (NPSI) Laboratory Directed Research and Development (LDRD) program at Pacific Northwest National Laboratory (PNNL). PNNL is a multiprogram national laboratory operated for the U.S. Department of Energy (DOE) by Battelle Memorial Institute under Contract No. DE-AC05-76RL0-1830. C.O. acknowledges support from the DOE Early Career Research Program. The STEM imaging shown was performed in the Radiological Microscopy Suite (RMS), located in the Radiochemical Processing Laboratory (RPL) at PNNL. Sample preparation was performed at the Environmental Molecular Sciences Laboratory (EMSL), a national scientific user facility sponsored by the Department of Energy's Office of Biological and Environmental Research and located at PNNL. *In situ* ion irradiation work was performed at the Center for Integrated Nanotechnologies, an Office of Science User Facility operated for the U.S. DOE. Sandia National Laboratories is a multimission laboratory managed and operated by National Technology and Engineering Solutions of Sandia, LLC, a wholly owned subsidiary of Honeywell International, Inc., for the U.S. DOE's National Nuclear Security Administration under contract DE-NA-0003525. Work at the Molecular Foundry was supported by the Office of Science, Office of Basic Energy Sciences, of the U.S. DOE under Contract DE-AC02-05CH11231.

REFERENCES

(1) Hwang, H. Y.; Iwasa, Y.; Kawasaki, M.; Keimer, B.; Nagaosa, N.; Tokura, Y. Emergent phenomena at oxide interfaces. *Nat. Mater.* **2012**, *11*, 103−113.

(2) Martin, L. W.; Rappe, A. M. Thin-film ferroelectric materials and their applications. *Nat. Rev. Mater.* **2017**, *2*, 16087.

(3) Huang, Z.; Ariando; Renshaw Wang, X.; Rusydi, A.; Chen, J.; Yang, H.; Venkatesan, T. Interface Engineering and Emergent Phenomena in Oxide Heterostructures. *Adv. Mater.* **2018**, *30*, 1802439.

(4) Fabbri, E.; Pergolesi, D.; Traversa, E. Ionic conductivity in oxide heterostructures: the role of interfaces. *Sci. Technol. Adv. Mater.* **2010**, *11*, 054503.

(5) Ismail-Beigi, S.; Walker, F. J.; Disa, A. S.; Rabe, K. M.; Ahn, C. H. Picoscale materials engineering. *Nat. Rev. Mater.* **2017**, *2*, 17060.

(6) Shamblin, J.; Feygenson, M.; Neuefeind, J.; Tracy, C. L.; Zhang, F.; Finkeldei, S.; Bosbach, D.; Zhou, H.; Ewing, R. C.; Lang, M. Probing disorder in isometric pyrochlore and related complex oxides. *Nat. Mater.* **2016**, *15*, 507−511.

(7) Gunkel, F.; Christensen, D. V.; Chen, Y. Z.; Pryds, N. Oxygen vacancies: The (in)visible friend of oxide electronics. *Appl. Phys. Lett.* **2020**, *116*, 120505.

(8) Zhang, Y. Y.; Mishra, R.; Pennycook, T. J.; Borisevich, A. Y.; Pennycook, S. J.; Pantelides, S. T. Oxygen Disorder, a Way to

Accommodate Large Epitaxial Strains in Oxides. *Adv. Mater. Interfaces* **2015**, *2*, 1500344.
(9) Hausmann, S.; Ye, J.; Aoki, T.; Zheng, J.-G.; Stahn, J.; Bern, F.; Chen, B.; Autieri, C.; Sanyal, B.; Esquinazi, P. D.; Böni, P.; Paul, A. Atomic-scale engineering of ferroelectric-ferromagnetic interfaces of epitaxial perovskite films for functional properties. *Sci. Rep.* **2017**, *7*, 10734.
(10) Shah, A. B.; Ramasse, Q. M.; May, S. J.; Kavich, J.; Wen, J. G.; Zhai, X.; Eckstein, J. N.; Freeland, J.; Bhattacharya, A.; Zuo, J. M. Presence and spatial distribution of interfacial electronic states in LaMnO3 - SrMnO3 superlattices. *Phys. Rev. B: Condens. Matter Mater. Phys.* **2010**, *82*, 115112.
(11) Varela, M.; Oxley, M.; Luo, W.; Tao, J.; Watanabe, M.; Lupini, A.; Pantelides, S.; Pennycook, S. Atomic-resolution imaging of oxidation states in manganites. *Phys. Rev. B: Condens. Matter Mater. Phys.* **2009**, *79*, 085117.
(12) MacManus-Driscoll, J. L.; Wells, M. P.; Yun, C.; Lee, J.-W.; Eom, C.-B.; Schlom, D. G. New approaches for achieving more perfect transition metal oxide thin films. *APL Mater.* **2020**, *8*, 040904.
(13) Brahlek, M.; Gupta, A. S.; Lapano, J.; Roth, J.; Zhang, H.-T. T.; Zhang, L.; Haislmaier, R.; Engel-Herbert, R. Frontiers in the Growth of Complex Oxide Thin Films: Past, Present, and Future of Hybrid MBE. *Adv. Funct. Mater.* **2018**, *28*, 1702772.
(14) Spurgeon, S. R. Order-disorder behavior at thin film oxide interfaces. *Curr. Opin. Solid State Mater. Sci.* **2020**, *24*, 100870.
(15) Zhang, X.; Hattar, K.; Chen, Y.; Shao, L.; Li, J.; Sun, C.; Yu, K.; Li, N.; Taheri, M. L.; Wang, H.; Wang, J.; Nastasi, M. Radiation damage in nanostructured materials. *Prog. Mater. Sci.* **2018**, *96*, 217−321.
(16) Beyerlein, I.; Caro, A.; Demkowicz, M.; Mara, N.; Misra, A.; Uberuaga, B. Radiation damage tolerant nanomaterials. *Mater. Today* **2013**, *16*, 443−449.
(17) Tuller, H. L.; Bishop, S. R. Point Defects in Oxides: Tailoring Materials Through Defect Engineering. *Annu. Rev. Mater. Res.* **2011**, *41*, 369−398.
(18) Ewing, R. C.; Weber, W. J.; Lian, J. Nuclear waste disposal-pyrochlore (A 2B 2O 7): Nuclear waste form for the immobilization of plutonium and "minor" actinides. *J. Appl. Phys.* **2004**, *95*, 5949−5971.
(19) Sickafus, K. E.; Minervini, L.; Grimes, R. W.; Valdez, J. A.; Ishimaru, M.; Li, F.; McClellan, K. J.; Hartmann, T. Radiation tolerance of complex oxides. *Science (Washington, DC, U. S.)* **2000**, *289*, 748−751.
(20) Cramer, T.; Sacchetti, A.; Lobato, M. T.; Barquinha, P.; Fischer, V.; Benwadih, M.; Bablet, J.; Fortunato, E.; Martins, R.; Fraboni, B. Radiation-Tolerant Flexible Large-Area Electronics Based on Oxide Semiconductors. *Adv. Electron. Mater.* **2016**, *2*, 1500489.
(21) George, E. P.; Raabe, D.; Ritchie, R. O. High-entropy alloys. *Nat. Rev. Mater.* **2019**, *4*, 515−534.
(22) Oses, C.; Toher, C.; Curtarolo, S. High-entropy ceramics. *Nat. Rev. Mater.* **2020**, *5*, 295−309.
(23) Vepsäläinen, A. P.; Karamlou, A. H.; Orrell, J. L.; Dogra, A. S.; Loer, B.; Vasconcelos, F.; Kim, D. K.; Melville, A. J.; Niedzielski, B. M.; Yoder, J. L.; Gustavsson, S.; Formaggio, J. A.; VanDevender, B. A.; Oliver, W. D. Impact of ionizing radiation on superconducting qubit coherence. *Nature* **2020**, *584*, 551−556.
(24) Was, G. S. Challenges to the use of ion irradiation for emulating reactor irradiation. *J. Mater. Res.* **2015**, *30*, 1158−1182.
(25) Odette, G.; Alinger, M.; Wirth, B. Recent Developments in Irradiation-Resistant Steels. *Annu. Rev. Mater. Res.* **2008**, *38*, 471−503.
(26) Meldrum, A.; Boatner, L.; Ewing, R. Effects of ionizing and displacive irradiation on several perovskite-structure oxides. *Nucl. Instrum. Methods Phys. Res., Sect. B* **1998**, *141*, 347−352.
(27) Lumpkin, G. R.; Smith, K. L.; Blackford, M. G.; Whittle, K. R.; Harvey, E. J.; Redfern, S. A. T.; Zaluzec, N. J. Ion Irradiation of Ternary Pyrochlore Oxides. *Chem. Mater.* **2009**, *21*, 2746−2754.
(28) Shamblin, J.; Tracy, C. L.; Ewing, R. C.; Zhang, F.; Li, W.; Trautmann, C.; Lang, M. Structural response of titanate pyrochlores to swift heavy ion irradiation. *Acta Mater.* **2016**, *117*, 207−215.
(29) Lang, M.; Zhang, F.; Zhang, J.; Wang, J.; Lian, J.; Weber, W. J.; Schuster, B.; Trautmann, C.; Neumann, R.; Ewing, R. C. Review of A2B2O7 pyrochlore response to irradiation and pressure. *Nucl. Instrum. Methods Phys. Res., Sect. B* **2010**, *268*, 2951−2959.
(30) Martínez, E.; Uberuaga, B. P.; Beyerlein, I. J. Atomic-Scale Studies of Defect Interactions with Homo- and Heterophase Interfaces. *JOM* **2016**, *68*, 1616−1624.
(31) Beyerlein, I.; Demkowicz, M.; Misra, A.; Uberuaga, B. Defect-interface interactions. *Prog. Mater. Sci.* **2015**, *74*, 125−210.
(32) Bai, X. M.; Voter, A. F.; Hoagland, R. G.; Nastasi, M.; Uberuaga, B. P. Efficient Annealing of Radiation Damage Near Grain Boundaries via Interstitial Emission. *Science (Washington, DC, U. S.)* **2010**, *327*, 1631−1634.
(33) Kreller, C. R.; Valdez, J. A.; Holesinger, T. G.; Morgan, J.; Wang, Y.; Tang, M.; Garzon, F. H.; Mukundan, R.; Brosha, E. L.; Uberuaga, B. P. Massively enhanced ionic transport in irradiated crystalline pyrochlore. *J. Mater. Chem. A* **2019**, *7*, 3917−3923.
(34) Spurgeon, S. R.; Kaspar, T. C.; Shutthanandan, V.; Gigax, J.; Shao, L.; Sassi, M. Asymmetric Lattice Disorder Induced at Oxide Interfaces. *Adv. Mater. Interfaces* **2020**, *7*, 1901944.
(35) Kaspar, T. C.; Gigax, J. G.; Shao, L.; Bowden, M. E.; Varga, T.; Shutthanandan, V.; Spurgeon, S. R.; Yan, P.; Wang, C.; Ramuhalli, P.; Henager, C. H. Damage evolution of ion irradiated defected-fluorite La2Zr2O7 epitaxial thin films. *Acta Mater.* **2017**, *130*, 111−120.
(36) Aguiar, J. A.; Dholabhai, P. P.; Bi, Z.; Jia, Q.; Fu, E. G.; Wang, Y. Q.; Aoki, T.; Zhu, J.; Misra, A.; Uberuaga, B. P. Linking Interfacial Step Structure and Chemistry with Locally Enhanced Radiation-Induced Amorphization at Oxide Heterointerfaces. *Adv. Mater. Interfaces* **2014**, *1*, 1300142.
(37) Aguiar, J. A.; Zhuo, M.; Bi, Z.; Fu, E.; Wang, Y.; Dholabhai, P. P.; Misra, A.; Jia, Q.; Uberuaga, B. P. Orientation-specific amorphization and intercalated recrystallization at ion-irradiated SrTiO3/MgO interfaces. *J. Mater. Res.* **2014**, *29*, 1699−1710.
(38) Dholabhai, P. P.; Aguiar, J. A.; Misra, A.; Uberuaga, B. P. Defect interactions with stepped CeO 2 /SrTiO 3 interfaces: Implications for radiation damage evolution and fast ion conduction. *J. Chem. Phys.* **2014**, *140*, 194701.
(39) Zhuo, M. J.; Fu, E. G.; Yan, L.; Wang, Y. Q.; Zhang, Y. Y.; Dickerson, R. M.; Uberuaga, B. P.; Misra, A.; Nastasi, M.; Jia, Q. X. Interface-enhanced defect absorption between epitaxial anatase TiO 2 film and single crystal SrTiO 3. *Scr. Mater.* **2011**, *65*, 807−810.
(40) Zhuo, M. J.; Uberuaga, B. P.; Yan, L.; Fu, E. G.; Dickerson, R. M.; Wang, Y. Q.; Misra, A.; Nastasi, M.; Jia, Q. X. Radiation damage at the coherent anatase interface under Ne ion irradiation. *J. Nucl. Mater.* **2012**, *429*, 177−184.
(41) Parrish, R. J.; Bufford, D. C.; Frazer, D. M.; Taylor, C. A.; Gutierrez-Kolar, J.; Buller, D. L.; Boyce, B. L.; Hattar, K. Exploring Coupled Extreme Environments via In-situ Transmission Electron Microscopy. *Micros. Microsc. Today* **2021**, *29*, 28−34.
(42) Ding, M. S.; Du, J. P.; Wan, L.; Ogata, S.; Tian, L.; Ma, E.; Han, W. Z.; Li, J.; Shan, Z. W. Radiation-Induced Helium Nanobubbles Enhance Ductility in Submicron-Sized Single-Crystalline Copper. *Nano Lett.* **2016**, *16*, 4118−4124.
(43) Li, J.; Yu, K. Y.; Chen, Y.; Song, M.; Wang, H.; Kirk, M. A.; Li, M.; Zhang, X. In situ study of defect migration kinetics and self-healing of twin boundaries in heavy ion irradiated nanotwinned metals. *Nano Lett.* **2015**, *15*, 2922−2927.
(44) Lian, J.; Wang, L.; Sun, K.; Ewing, R. C. In situ TEM of radiation effects in complex ceramics. *Microsc. Res. Tech.* **2009**, *72*, 165−181.
(45) Birtcher, R.; Kirk, M.; Furuya, K.; Lumpkin, G.; Ruault, M.-O. In situ Transmission Electron Microscopy Investigation of Radiation Effects. *J. Mater. Res.* **2005**, *20*, 1654−1683.
(46) Ye, B.; Kirk, M. A.; Chen, W.; Oaks, A.; Rest, J.; Yacout, A.; Stubbins, J. F. TEM investigation of irradiation damage in single crystal CeO2. *J. Nucl. Mater.* **2011**, *414*, 251−256.
(47) Zhang, Y.; Lian, J.; Wang, C. M.; Jiang, W.; Ewing, R. C.; Weber, W. J. Ion-induced damage accumulation and electron-beam-

https://doi.org/10.1021/acs.nanolett.1c01651
Nano Lett. 2021, 21, 5353−5359

enhanced recrystallization in SrTiO3. *Phys. Rev. B: Condens. Matter Mater. Phys.* **2005**, *72*, 1−8.
(48) Wang, L. M. Applications of advanced electron microscopy techniques to the studies of radiation effects in ceramic materials. *Nucl. Instrum. Methods Phys. Res., Sect. B* **1998**, *141*, 312−325.
(49) Zinkle, S. J.; Hodgson, E. R. Radiation-induced changes in the physical properties of ceramic materials. *J. Nucl. Mater.* **1992**, *191*−*194*, 58−66.
(50) Spurgeon, S.; Chambers, S. *Encyclopedia of Interfacial Chemistry*; Elsevier: New York, 2018; pp 38−48.
(51) Hattar, K.; Jungjohann, K. L. Possibility of an integrated transmission electron microscope: enabling complex in-situ experiments. *J. Mater. Sci.* **2021**, *56*, 5309−5320.
(52) Spurgeon, S. R.; et al. Towards data-driven next-generation transmission electron microscopy. *Nat. Mater.* **2021**, *20*, 274−279.
(53) Taheri, M. L.; Stach, E. A.; Arslan, I.; Crozier, P. A.; Kabius, B. C.; LaGrange, T.; Minor, A. M.; Takeda, S.; Tanase, M.; Wagner, J. B.; Sharma, R. Current status and future directions for in situ transmission electron microscopy. *Ultramicroscopy* **2016**, *170*, 86−95.
(54) Hÿtch, M.; Snoeck, E.; Kilaas, R. Quantitative measurement of displacement and strain fields from HREM micrographs. *Ultramicroscopy* **1998**, *74*, 131−146.
(55) Ophus, C. Four-Dimensional Scanning Transmission Electron Microscopy (4D-STEM): From Scanning Nanodiffraction to Ptychography and Beyond. *Microsc. Microanal.* **2019**, *25*, 563−582.
(56) Savitzky, B. H.; et al. py4DSTEM: A Software Package for Four-Dimensional Scanning Transmission Electron Microscopy Data Analysis. *Microsc. Microanal.* **2021**, 1−32.
(57) Janish, M. T.; Schneider, M. M.; Ophus, C.; Ciston, J.; Valdez, J. A.; McClellan, K. J.; Byler, D. D.; Chen, D.; Wang, Y.; Holesinger, T. G.; Uberuaga, B. P. Mapping Cation Disorder in Irradiated Gd 2 Ti 2 O 7 Pyrochlore by 4D-STEM. *Microsc. Microanal.* **2019**, *25*, 1560−1561.
(58) Jiang, W.; Van Ginhoven, R. M.; Kovarik, L.; Jaffe, J. E.; Arey, B. W. Superlattice structure and precipitates in O + and Zr + ion coimplanted SrTiO 3: A model waste form for 90Sr. *J. Phys. Chem. C* **2012**, *116*, 16709−16715.
(59) Kaspar, T. C.; Sushko, P. V.; Spurgeon, S. R.; Bowden, M. E.; Keavney, D. J.; Comes, R. B.; Saremi, S.; Martin, L.; Chambers, S. A. Electronic Structure and Band Alignment of LaMnO 3 /SrTiO 3 Polar/Nonpolar Heterojunctions. *Adv. Mater. Interfaces* **2019**, *6*, 1801428.

https://doi.org/10.1021/acs.nanolett.1c01651
Nano Lett. 2021, 21, 5353−5359